Intensified proton and carbon ion flux from femtosecond laser driven plasma source

P. K. Singh,[1] A. A. Andreev,[2,3] K. F. Kakolee,[1] and S. Ter-Avetisyan[2,a)]
[1]*Center for Relativistic Laser Science, Institute for Basic Science, Gwangju 61005, Korea*
[2]*ELI-ALPS, Szeged H-6728, Hungary*
[3]*St. Petersburg State University, St. Petersburg 199034, Russia*

(Received 28 August 2018; accepted 1 November 2018; published online 26 November 2018)

Ion acceleration from aluminium foils irradiated with a 30 fs laser pulse of $\sim 10^{20}$ W/cm^2 intensity at an incidence angle of 45° was investigated. Laser intensity contrast enhancement by a factor of 100 resulted in a nearly 7 and 30 times increase in proton and carbon ion flux, respectively, while their maximum energy remains almost unchanged. More than 10^{13} protons and 10^{14} carbon C^{4+} ions per MeV bandwidth per steradian solid angle were measured. Simulations, being in a good agreement with the experimental findings, have revealed that the difference in proton emission between the low and high contrast cases is a narrower angular distribution of protons at high laser pulse contrast. In the low contrast scenario, the plasma density gradient increases the hot electron divergence, leading to the reduction of particle flux in a fixed solid angle. The analytical model verifies the concept of the theoretical limit of particle flux. These results open up the possibility for further optimization of the laser driven bright source of energetic particles. *Published by AIP Publishing.*
https://doi.org/10.1063/1.5053964

I. INTRODUCTION

The interaction of intense ultrashort laser pulse with thin solid foil leads to the acceleration of multi-MeV ion beams with unique properties including low emittance, high brilliance, and ultrashort duration, making them attractive for many prospective applications.[1] Despite that the current beam parameters required for applications have yet to be achieved, laser-driven ion beams have already found applications in a wide range of areas, e.g., probing of fields in plasmas,[2] generation of directional neutron sources,[3] isochoric heating of solid matter,[4] and radiobiology, where high-current and short-bunch make possible time-resolved determination of radical yields.[5–7]

The successful realisation of the above applications relies on reproducible ion sources with high particle energy and flux. While there are various novel ion acceleration mechanisms,[1] the well-established so-called target normal sheath acceleration (TNSA) mechanism has proven being capable of reproducibly generating relatively high flux of energetic particles under a vast range of laser and target parameters.[8–10] However, ion beams generated by the TNSA mechanism have a wide energy spread and a large divergence, whereas almost all potential applications depend on the production of nearly mono-energetic, collimated particle bunches. For instance, beam transport in new compact accelerators[11,12] would greatly benefit from a mono-energetic spectrum; the resolution and contrast of imaging radiography[4,13] can be further improved. From this perspective, if there is enough high particle flux in the beam, it was shown that a mono-energetic proton beam can be selected from the broad spectrum of particles and collimated or further focused, e.g., using a quadrupole-magnet-lens system,[14] as required for applications.

This paper presents the recent results on laser acceleration of ions from thin (few micrometres thick) aluminium foils where the measured particle flux was the highest so far in the short laser pulse experiments. Moreover, there was nearly 7 times enhancement in the proton flux and 30 times enhancement in the carbon ion flux after improving the laser pulse contrast by almost two orders of magnitude. This occurred with almost no change in maximum ion energies. The dependence of the measured maximum ion energies on their charge-to-mass ratio indicates that all ions are subjected to the same accelerating field. The obtained high flux of ion beams may open new perspectives for applications, and the significance of these beams for ultrafast heating of matter is given as an example.

II. EXPERIMENTAL SETUP

Experiments were performed with the 100 TW Ti:Sa femtosecond laser system.[15] Figure 1(a) shows the experimental layout. A *p*-polarized, 30 fs laser pulse with energy of nearly 3 J was focused using an f/2 dielectric off-axis parabolic mirror onto a 2 μm thick Al foil at an incidence angle of 45°. The energy distribution of the laser focal spot is shown in Fig. 1(b). Nearly 50% of laser energy confined in the diffraction limited area of the focal spot results in an intensity of $(2 \pm 1) \times 10^{20}$ W/cm^2. The uncertainty in laser intensity calculation is connected with the estimate of the fractional laser energy content in the focal area. During the experiment, laser intensity contrasts of 10^{-8} and 10^{-10} at few ps before the main pulse were employed, denoting as low-contrast and high-contrast modes, respectively, by inserting a saturable absorber (RG-850) between the front-end and the stretcher in

a)Author to whom correspondence should be addressed: sargis.ter-avetisyan@eli-alps.hu

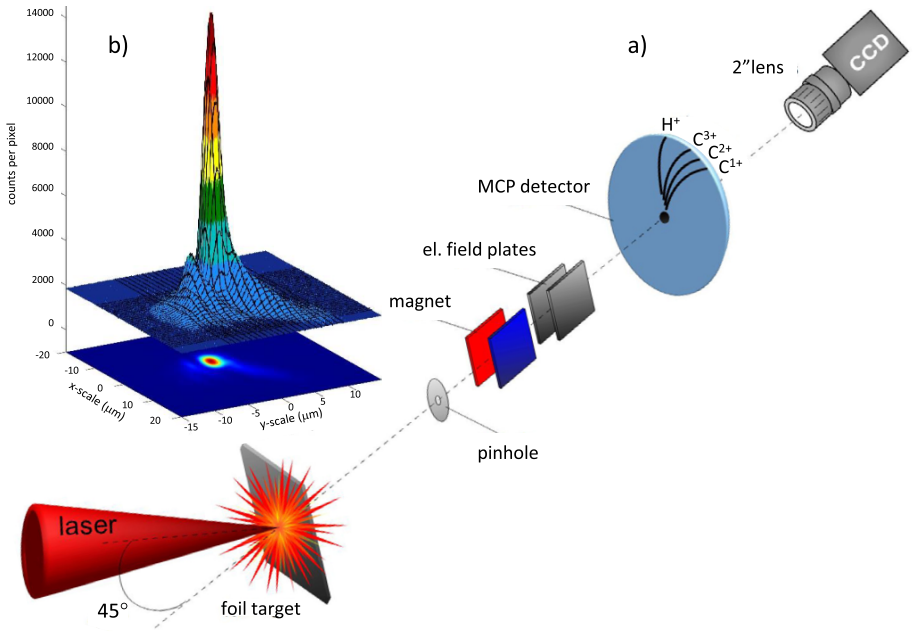

FIG. 1. (a) The sketch of the experimental setup. A laser accelerated ion beam is formed by the entrance pinhole of the Thomson spectrometer where particles are deflected according to their mass-to-charge ratio in the parallel magnetic and electric fields. On a MCP detector, the particle spectra appear as parabolic traces and CCD takes a snapshot from the phosphor screen of MCP. (b) Intensity distribution of the laser focal spot.

the laser system. The nanosecond pedestal in the system was well below 10^{-12}.[15]

A laser focal spot and target positioning diagnostic system, with an accuracy of few micrometers, was used for the precise alignment of thin foils at the laser focal plane.[16] An absolutely calibrated Thomson spectrometer with a microchannel-plate (MCP) detector was installed along the rear surface target normal direction.[17] Ion spectra have been dispersed in parallel magnetic (0.8 ± 0.1 T) and electric fields (16 kV/cm) [Fig. 1(a)]. A 100 μm entrance pinhole of the spectrometer with an acceptance solid angle of $\sim 10^{-8}$ sr ensured clear separation of ion species and high energy resolution ($\sim$ 0.7% at 20 MeV/nucleon). The spectra were analysed using the MATLAB code. During the experiment, Al targets with thicknesses of 0.4 and 2.0 μm were used. The ions mainly from the native contaminant layer present at the surface of the target rather than the ions from the target bulk have been accelerated due to their high charge-to-mass ratio. The ion spectra did not show a significant dependence on target thickness.

Typical parabolic spectral traces of ions, measured using a Thomson spectrometer,[17] are shown in Figs. 2(a) and 2(b) for high and low laser pulse contrasts, respectively, under a similar laser irradiance of 2×10^{20} W/cm^2 of the 2 μm Al target. The corresponding evaluated spectra of protons and C^{4+} ions are shown in Figs. 2(c) and 2(d). A drastic enhancement in the ion flux is observed by changing the laser intensity contrast by two orders of magnitude (from 10^{-8} to 10^{-10}).

III. EXPERIMENTAL RESULTS

Special precautions have been taken for the estimation of the absolute number of particles from the charged-coupled-device (CCD) image of ion spectra. A precise absolute calibration of the whole detection system has been performed.[17] It should be considered that, in the spectrometer setup, the projected image of the pinhole as a width of the parabolic trace is a faithful reproduction of the object as was seen on the CR-39 track detector that gave the exact image of the pinhole at high and low particle fluxes.[18] However, on the CCD image, it critically varies on whether the centre of the image projection falls on the centre of a pixel or at the vertex of pixels. As a result, a larger area of the CCD relative to the pinhole image size is affected. Additionally, increasing the particle flux and the signal level on MCP results in even a larger affected area on CCD, and the pinhole image is not adequate. The width of the parabolic trace in images appears to be about 300 μm FWHM, while the imaging pinhole has only a size of 100 μm. This is in contrast to the "low signal" case, where the image of the pinhole is perfectly reproduced. In the analysis, the affected area of the CCD image outside of pinhole image size was taken as the background signal and subtracted from the signal within the area of about 100 μm along the trace. Following this procedure, the possible minimum number of particles was estimated.

The proton spectrum with high laser pulse contrast (10^{-10}) shows a seven times enhancement of the proton flux in the (1.5–6.0) MeV energy interval [Fig. 2(c)], and there is an approximately 30 times flux enhancement for carbon ions (C^{4+}) in the (2–10) MeV energy interval [Fig. 2(d)]. At high- and low-contrast cases, the maximum proton and C^{4+} energies stay nearly unchanged: protons $E_{max} \sim 10$ MeV and $C^{4+} \sim 13$ MeV ($\sim$1 MeV/nucleon). A small difference in energies for carbon ions at low- and high-contrast cases could also be due to the scarce particle count in a high-energy tail of the spectra.

Figure 3 compares these proton fluxes with previously reported experimental results from the literature[19–24] at optimum interaction conditions. To the best of our knowledge, these are the data available in the literature so far for 50 fs or shorter laser pulses but for various intensities. Obviously, the observation of a high number of particles more than an order of magnitude in the present experiments as compared to the

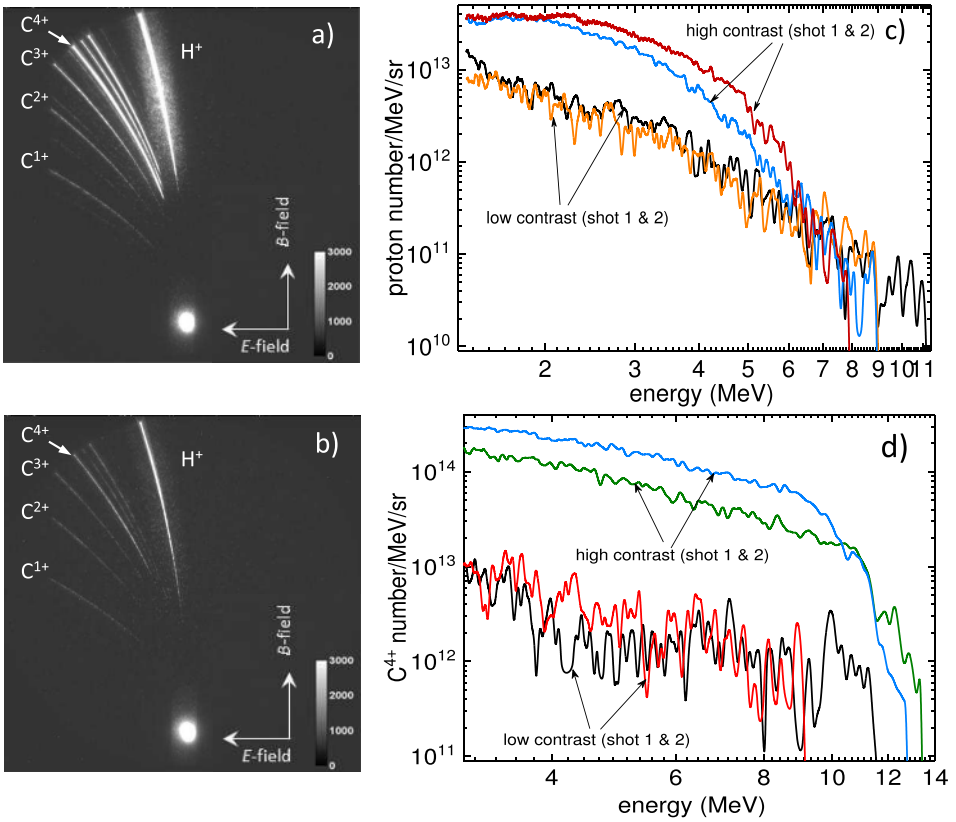

FIG. 2. Parabolic spectral traces of accelerated ions for (a) high-contrast (10^{-10}) and (b) low-contrast (10^{-8}) cases. (c) A comparison of the proton energy spectra relevant to low- and high-contrast cases for two consecutive shots. (d) Comparison of carbon ion (C^{4+}) energy spectra relevant to low- and high-contrast cases for two consecutive shots.

literature results suggests that the interaction scenario might be changing when a high intensity laser interacts with a steep target density gradient.

IV. NUMERICAL SIMULATIONS OF THE PROTON DENSITY PROFILE

2D particle-in-cell (PIC) simulations have been performed to reproduce the experimental observations and reveal the phenomena responsible for increased proton flux. In the simulation, a p-polarized, 30 fs laser pulse is focused at an intensity of 2×10^{20} W/cm^2 to a 4 μm spot on a 2 μm Al^{10+} target with 40 nm contaminant layers at an incidence angle of 45°. The simulation box of 25×25 μm^2 contained 5000×5000 cells with 30 particles per cell and with a step of 5 nm. Two types of interactions have been considered: (i) 2 μm target with a rectangular density profile that corresponds to a high contrast interaction and (ii) with a 0.5 μm density gradient at the front of the 1.5 μm thick target corresponding to the low contrast case. The number of particles was the same in both cases. The simulation lasts up to 128 fs, where protons are accelerated and the spectrum is close to saturation (at about 170 fs).

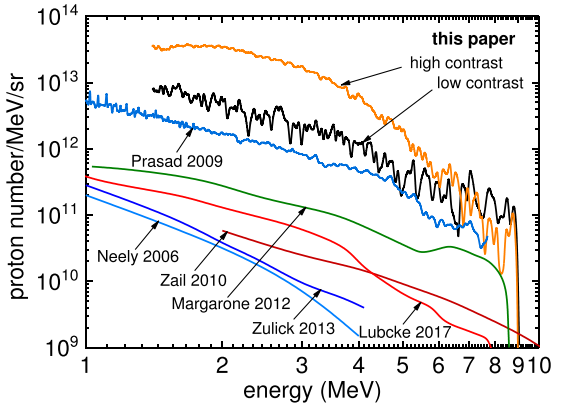

FIG. 3. Comparison of proton flux measured in this study with the results reported in the literature: Neely 2006,[19] Prasad 2009,[20] Zeil 2010,[21] Margarone 2012,[22] Zulick 2013,[23] and Lubcke 2017.[24]

The density profile of protons and the corresponding phase diagrams are shown in Fig. 4 for the high [(a) and (c)] and low [(b) and (d)] laser pulse contrasts. The difference between these two cases is the much narrow angular distribution of protons and higher density in the case of high laser pulse contrast. Consequently, a substantial amount of high number of protons will be recorded through a 100 μm entrance pinhole of the spectrometer in the high laser pulse contrast case as measured in the experiments. In simulations, the number of particles is restricted, and the spectrum in a solid angle similar to the experiments (in 10^{-8} sr) cannot be obtained in reasonable computational time since the number of particles has to be increased by several orders of magnitude. The simulated distribution functions of the protons at an angle of $\pm 2°$ with respect to the target normal for the different plasma inhomogeneity scale-lengths L: black line $L = 0$ (high contrast) and red line: $L = 0.5$ μm (low contrast) at 213 fs after the interaction (Fig. 5) show proton flux enhancement at high laser contrast conditions, while maximum proton energies were similar. The decrease in proton beam divergence at high laser pulse contrast was also indirectly observed in Ref. 8 and was estimated to be ~8°, and a decrease in beam divergence from 20° to <10° was measured in Ref. 25, when the laser contrast was increased through the use of double plasma mirror.

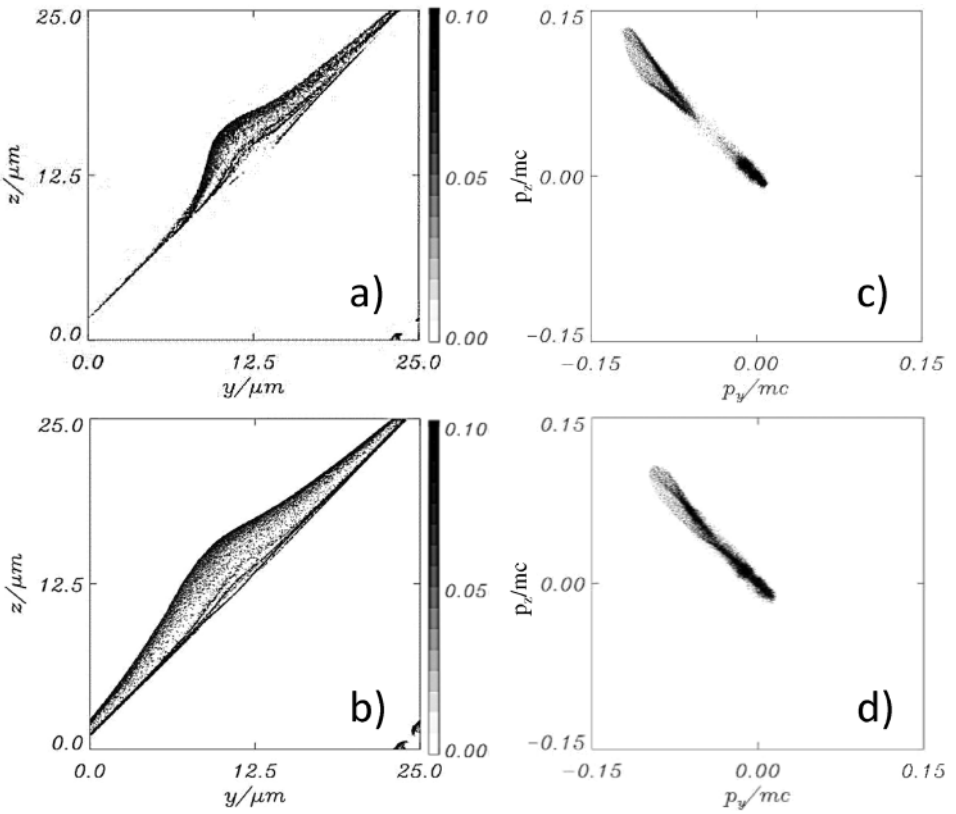

FIG. 4. The density profile of protons [(a) and (b)] and its phase diagrams [(c) and (d)] are shown for the "high" [(a) and (c)] and "low" [(b) and (d)] laser pulse contrasts.

At the temporal contrast of $\sim 10^{-10}$, the prepulse intensity would be $\sim 2 \times 10^{10}$ W/cm^2 at a few ps before the main pulse. Estimating the velocity of the Al ions to be $\sim 10^6$ cm/s,[26] the preplasma can only reach an extension of a few tenths of nm before the arrival of the main pulse. Therefore, the high contrast level of the laser system prevents the formation of any significantly extended preplasma at the target front surface.

V. ANALYTICAL MODEL OF ION FLUX ENHANCEMENT THROUGH ACCELERATION IN A FIELD OF CHARGE CAVITY

At high intensity and high contrast laser pulse, the ponderomotive force pushes the electrons deep into a foil target in the form of moving electron density spike.[10] This produces a charge separation cavity at the target front with a radius similar to the laser beam radius at the focus r_L and length l_s.[27,28] The electron spike experiences a strong restoring electrostatic field due to the charged layer left behind, unless a balance between the Coulomb force and the ponderomotive force is achieved. Such a balance gives a rough estimate of the nonlinear relativistic skin depth

$$l_s(l) \approx \left(\frac{l_s}{1 + l_0/l} + \frac{l_s}{1 + l/l_0} \right), \tag{1}$$

as the interpolation of two limits: $l_{1s}(l) \approx c/\omega_{pe}$ at $l > l_0$ and $l_{2s} \approx \frac{c}{\omega_{pe}} \frac{\omega^2}{\omega_{pe}^2} a$ at $l < l_0$, where $l_0 = c\omega a/2\omega_{pe}^2$ is a characteristic transparency length, l is the foil thickness, ω and ω_{pe} are the laser and electron plasma wave frequencies, respectively, and $a = eE_L/m\omega c$ is the normalized laser electric field amplitude E_L.

The laser accelerated electrons propagate along the normal to the surface of this charged cavity, and the divergence angle of fast electrons can be estimated as $\theta_d \approx l_s/r_L$[29,30] for a steep target density profile (high-contrast) as a low limit of the electron divergence. For the overdense plasma with density gradient L (low-contrast), the divergence would be $\theta_d \approx L \ln a/r_L$. The density gradient L can be estimated from a simple hydro-model as $L \approx c_s t_{pL}$, where c_s is the ion sound velocity and t_{pL} is the laser pre-pulse duration. These divergent electron beams generate an inhomogeneous electric field at foil rear, which accelerates the divergent ion beam.

The number of ions propagating through a pinhole of the spectrometer N_i depends on its divergence angle θ_d. Therefore, the ratios of the number of particles reaching the

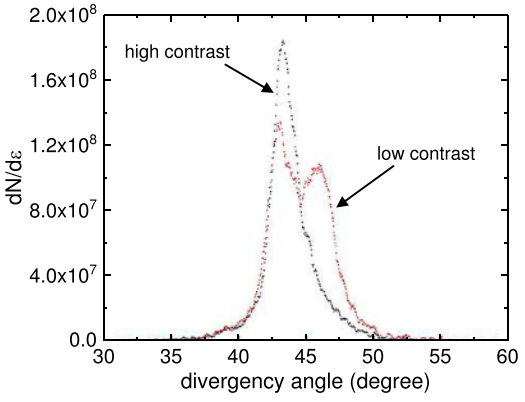

FIG. 5. The simulated energy distribution functions of the protons propagating at the angle of ±2° with respect to the target normal for the different plasma inhomogeneity scale-lengths L at the time moment of 213 fs. Black line: $L = 0$ (high contrast) and red line: $L = 0.5\,\mu$m (low contrast). The angle of 45° means normal to the target.

detector for laser pulses with low (N_{il}) and high (N_{ih}) contrasts can be written as

$$N_{ih}/N_{il} \approx (\theta_{dh}/\theta_{dl})^2 \approx (L_l/L_h)^2, \tag{2}$$

where θ_{dh} or θ_{dl} and L_h or L_l are the ion divergences and the plasma density gradients for high and low contrast laser pulses, respectively. To determine L_h or L_l, the prepulse durations are assumed to be the same for both scenarios $t_{pL}^{(l)} \approx t_{pL}^{(h)}$, but the prepulse intensities are different $I_{pL}^{(l)} \approx 100 \cdot I_{pL}^{(h)}$. Using the standard dependencies $c_s \approx \sqrt{T_e/T_{e0}} \cdot c_{s0}$ and $T_e \approx \sqrt{I_{pL}/I_0} \cdot T_{e0}$, where c_{s0}, T_{e0}, and I_0 are constants, one can get L_h or $L_l \approx L_0 \cdot \left(I_{pL}^{(l\,or\,h)}\right)^{1/4}$, where L_0 is the normalization constant. Inserting it into the formula (2) results in

$$N_{ih}/N_{il} \approx \sqrt{I_{pL}^{(l)}/I_{pL}^{(h)}} \approx 10, \tag{3}$$

which is by the order of magnitude comparable with the experimental results.

Nearly identical maximum proton energy for both conditions of laser pulse contrasts suggests that the laser pulse drives similarly the maximum of the field and the small preplasma affects only the electron divergence inside the target. The latter also makes electron recirculation, which sustains the accelerating sheath field, less effective.[31] A small transverse velocity component is enough to move electrons out of the interaction region.

The spectra of multiple ion species (H^+, $C^{5+} - C^{1+}$, and O^{6+}) evaluated from Fig. 2(a) are plotted in Fig. 6(a). Figure 6(b) shows a data collection of maximum energy of various ion species dependent on their charge-to-mass ratio (q/m) measured at different laser shots. The variation in the dataset for a given species is due to inherent shot-to-shot fluctuations in the laser-matter interaction conditions—the laser pulse contrast and local target parameters. The target was positioned at the laser focal plane with the accuracy of few μm.[16] The shot-to-shot fluctuation of the amplified laser pulse energy had a $< 1\%$ rms value in a single laser shot mode. The overall variation of maximum proton energy is $\sim 15\%$.

In Fig. 6(b), the scaling of maximum ion energy with a q/m ratio is fitted with the analytical model describing the electrostatic field formation at the target rear by the laser-accelerated electrons.[32] The electrons from the laser focal spot of radius r_L propagate through the target of thickness l with a divergence half-angle of θ (assumed to be 30°) to the target rear and uniformly fill a circular region of radius $R = r_L + l \times \tan(\theta)$. In this model, the maximum ion energy (E_{max}) is given on the base of radially confined surface charge on the target rear and can be found from the following expression:

$$\frac{\tau_L}{\tau_0} = X\left(1 + \frac{1}{2}\frac{1}{1-X^2}\right) + \frac{1}{4} ln \frac{1+X}{1-X}, \tag{4}$$

where τ_L is the laser pulse duration, $\tau_0 = R/v_\infty$, v_∞ is the maximum ion velocity, $X = (E_{max}/E_\infty)^{1/2}$, and E_∞

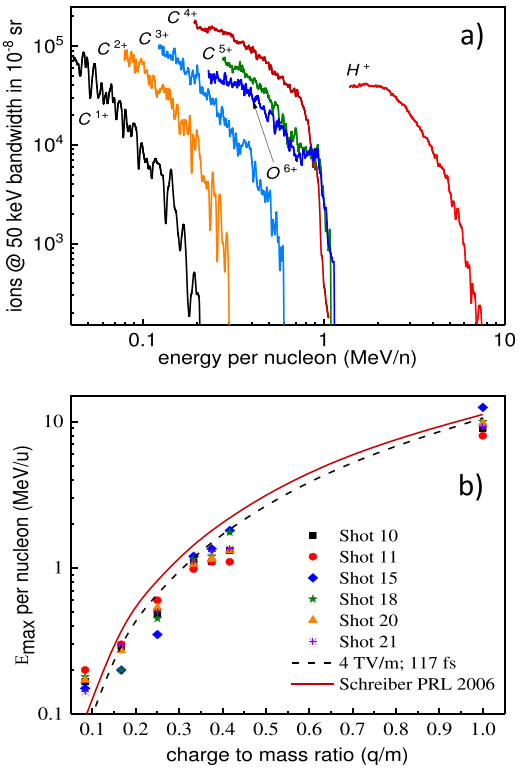

FIG. 6. (a) Energy spectrum of accelerated ions. (b) Dependence of maximum energy of ion species per nucleon on their charge to mass ratios (q/m). The red solid line is a calculation based on the model described by Schreiber *et al.*,[31] and the dashed black line indicates the energy gained by ions accelerated in a sheath field of 4 TV/m within 117 fs.

$= q_i 2 m_e c^2 (\eta P_L/P_R)^{1/2}$, where P_L is the laser power, $P_R = 8.7\,GW$ is the relativistic power, q_i is the ion charge, and η is the laser to fast electron energy conversion efficiency (assumed 35% in this study). The dependence of the maximum ion energy on q/m can also be tested by a simple assumption that all ion species are accelerated under similar electrostatic field present for $\tau = 117$ fs ($\tau = 1.3 \times \tau_L + 78 fs$).[33]

The value of the electric field, found from the curve fitting of all the dataset in Fig. 6(b), is nearly 4 TV/m. This field strength explains the dominance of C^{4+} ion flux over the other carbon species [see Fig. 6(a)]. The electric field required for the field ionization of a given species is $E_{FI} = \pi \varepsilon U_{q_i}^2 / q_i e$, where ε is the vacuum permittivity, U_{q_i} is the ionization potential of the ion, and e is the electron charge. For $C^{4+}(U_Q = 64.4\,\text{eV})$, the required field for ionization is 0.14 TV/m, and for $C^{5+}(U_Q = 392\,\text{eV})$, the field ionization threshold is 5.3 TV/m. Interestingly, the estimated sheath field (4 TV/m) is only about one order of magnitude weaker than the laser electric field (~ 30 TV/m).

VI. ION BEAMS FOR WARM-DENSE-MATTER STUDIES

The measured ion flux can be of potential use in various applications. The significance of the obtained ion flux for ultrafast heating of matter is demonstrated below as an example. By taking the reference spectrum shown in Fig. 6(a), the particle flux in the 50 keV bandwidth at 2 MeV proton and 3 MeV carbon (C^{4+}) ions is nearly 2×10^4 and

TABLE I. Estimation of average heating temperature by irradiation of proton and carbon C^{4+} ion beams.

Species	Energy (MeV)	Flux at 50 keV bandwidth in 10^{-9} sr	Heating foil distance (μm)	Stopping range (μm)	Heated volume (μm^3)	Estimated temperature (eV)
Proton	2	2×10^4	1500	18.4	4.0×10^6	1.2
C^{4+}	3	1×10^5	1500	1.7	0.4×10^6	94.8

1×10^5, respectively. The full divergence of the ion beam is assumed to be 20°. The stopping range of particles, e.g., in copper, from the SRIM code[34] is given in Table I. The average absorbed energy per heating target atom (T_{avg}) is estimated as follows:

$$T_{avg} = (N_{incident} \times E_{incident})/N_{Heating}, \quad (5)$$

where $N_{incident}$ and $E_{incident}$ are the total number of incident ions on the target and their energy, respectively, and $N_{Heating}$ is the total number of heated target atoms. The results, summarized in Table I, demonstrate the potential of the bright MeV ion flux in ultrafast heating of targets for warm-dense matter studies. The dominance of the carbon ion over the proton at heated temperature is due to much higher particle flux and a shorter stopping range.

VII. SUMMARY

In conclusion, the highest particle flux measured so far in the short laser pulse experiments at the interaction of an ultraintense and high contrast laser pulse with a foil target has been demonstrated. Moreover, the flux of accelerated proton and carbon ion beams is significantly increased when a high-contrast laser pulse is applied. An estimate of the absolute minimum number of protons above 10^{13} and for carbon, C^{4+}, above 10^{14} particles per MeV bandwidth per sr solid angle has been obtained. Furthermore, there is a near seven times enhanced proton and 30 times enhanced carbon ion flux when the laser pulse contrast is increased. 2D particle-in-cell simulations have demonstrated the narrowing of the angular distribution of protons when the laser pulse contrast is changed from low to high values. In the low contrast scenario, the long-scale plasma density gradient increases the hot electron divergence, and therefore, the particle flux at a given solid angle decreases. The analytical model verifies the concept of the theoretical limit of particle flux enhancement due to the divergence limit of fast electrons propagating along the normal to the surface of charged cavity created at the target front (steep density profile—high contrast case). The measurement of the small angles of ion beam divergence is an experimental challenge. Perhaps, the "tomographic approach" can be applied[35] for such a measurement, which will be a topic of another investigation. These results open a possibility for further optimization of laser driven bright sources of energetic particles.

ACKNOWLEDGMENTS

This work was performed under the ELI-ALPS Project (No. GINOP-2.3.6-15-2015-00001) supported by the European Union and co-financed by the European Regional Development fund and by the Institute for Basic Science under IBS-R012-D1. We thank T. W. Jeong for the support during the experiments and S. Sharif for data analysis.

[1]A. Macchi, M. Borghesi, and M. Passoni, Rev. Mod. Phys. **85**, 751 (2013).
[2]M. Borghesi, D. H. Campbell, A. Schiavi, M. G. Haines, O. Willi, A. J. MacKinnon, P. Patel, L. A. Gizzi, M. Galimberti, R. J. Clarke, F. Pegoraro, H. Ruhl, and S. Bulanov, Phys. Plasmas **9**, 2214 (2002).
[3]S. Kar, A. Green, H. Ahmed, A. Alejo, A. P. L. Robinson, M. Cerchez, R. Clarke, D. Doria, S. Dorkings, J. Fernandez, S. R. Mirfayzi, P. McKenna, K. Naughton, D. Neely, P. Norreys, C. Peth, H. Powell, J. A. Ruiz, J. Swain, O. Willi, and M. Borghesi, New J. Phys. **18**, 053002 (2016).
[4]A. Pelka, G. Gregori, D. O. Gericke, J. Vorberger, S. H. Glenzer, M. M. Günther, K. Harres, R. Heathcote, A. L. Kritcher, N. L. Kugland, B. Li, M. Makita, J. Mithen, D. Neely, C. Niemann, A. Otten, D. Riley, G. Schaumann, M. Schollmeier, A. Tauschwitz, and M. Roth, Phys. Rev. Lett. **105**, 265701 (2010).
[5]A. Yogo, K. Sato, M. Nishikino, M. Mori, T. Teshima, H. Numasaki, M. Murakami, Y. Demizu, S. Akagi, S. Nagayama, K. Ogura, A. Sagisaka *et al.*, Appl. Phys. Lett. **94**, 181502 (2009).
[6]S. D. Kraft, C. Richter, K. Zeil, M. Baumann, E. Beyreuther, S. Bock, M. Bussmann, T. E. Cowan, Y. Dammene, W. Enghardt, U. Helbig *et al.*, New J. Phys. **12**, 085003 (2010).
[7]S. Raschke, S. Spickermann, T. Toncian, M. Swantusch, J. Boeker, U. Giesen, G. Iliakis, O. Willi, and F. Boege, Sci. Rep. **6**, 32441 (2016).
[8]R. Prasad, A. A. Andreev, S. Ter-Avetisyan, D. Doria, K. E. Quinn, L. Romagnani, C. M. Brenner, D. C. Carroll, N. P. Dover, D. Neely, P. S. Foster *et al.*, Appl. Phys. Lett. **99**, 121504 (2011).
[9]F. Wagner, O. Deppert, C. Brabetz, P. Fiala, A. Kleinschmidt, P. Poth, V. A. Schanz, A. Tebartz, B. Zielbauer, M. Roth, T. Stöhlker, and V. Bagnoud, Phys. Rev. Lett. **116**, 205002 (2016).
[10]V. Y. Bychenkov, P. K. Singh, H. Ahmed, K. F. Kakolee, C. Scullion, T. W. Jeong, P. Hadjisolomou, A. Alejo, S. Kar, M. Borghesi, and S. Ter-Avetisyan, Phys. Plasmas **24**, 010704 (2017).
[11]D. Habs, G. Pretzler, A. Pukhov, and J. Meyer-ter-Vehn, Prog. Part. Nucl. Phys. **46**, 375 (2001).
[12]P. Antici, M. Fazi, A. Lombardi, M. Migliorati, L. Palumbo, P. Audebert, and J. Fuchs, J. Appl. Phys. **104**, 124901 (2008).
[13]J. A. Cobble, R. P. Johnson, T. E. Cowan, N. Renard-Le Galloudec, and M. Allen, J. Appl. Phys. **92**, 1775 (2002).
[14]S. Ter-Avetisyan, M. Schnürer, R. Polster, P. V. Nickles, and W. Sandner, Laser Part. Beams **26**, 637 (2008).
[15]J. H. Sung, S. K. Lee, T. M. Jeong, and C. H. Nam, Appl. Phys. B **116**, 287 (2014).
[16]P. K. Singh, K. F. Kakolee, T. W. Jeong, and S. Ter-Avetisyan, Nucl. Instrum. Methods Phys. Res. A **829**, 363 (2016).
[17]T. W. Jeong, P. K. Singh, C. Scullion, H. Ahmed, K. F. Kakolee, P. Hadjisolomou, A. Alejo, S. Kar, M. Borghesi, and S. Ter-Avetisyan, Rev. Sci. Instrum. **87**, 083301 (2016).
[18]T. W. Jeong, P. K. Singh, C. Scullion, H. Ahmed, P. Hadjisolomou, C. Jeon, H. Yun, K. F. Kakolee, M. Borghesi, and S. Ter-Avetisyan, Sci. Rep. **7**, 2152 (2017).
[19]D. Neely, P. Foster, A. Robinson, F. Lindau, O. Lundh, A. Persson, C.-G. Wahlström, and P. McKenna, Appl. Phys. Lett. **89**, 021502 (2006).
[20]R. Prasad, Private communication, experiments on GEMINI laser within LIBRA project, 0.1 μm Al target, 35° laser incidence, intensity of 1.3×10^{20} W/cm^2, shot number 458 (2009).
[21]K. Zeil, S. D. Kraft, S. Bock, M. Bussmann, T. E. Cowan, T. Kluge, J. Metzkes, T. Richter, R. Sauerbrey, and U. Schramm, New J. Phys. **12**, 045015 (2010).
[22]D. Margarone, O. Klimo, I. J. Kim, J. Prokůpek, J. Limpouch, T. M. Jeong, T. Mocek, J. Pšikal, H. T. Kim, J. Proška, K. H. Nam, L. Štolcová, I. W. Choi, S. K. Lee, J. H. Sung, T. J. Yu, and G. Korn, Phys. Rev. Lett. **109**, 234801 (2012).

[23]C. Zulick, F. Dollar, V. Chvykov, J. Davis, G. Kalinchenko, A. Maksimchuk, G. M. Petrov, A. Raymond, A. G. R. Thomas, L. Willingale, V. Yanovsky, and K. Krushelnick, Appl. Phys. Lett. **102**, 124101 (2013).
[24]A. Lubcke, A. A. Andreev, S. Hohm, R. Grunwald, L. Ehrentraut, and M. Schnürer, Sci. Rep. **7**, 44030 (2017).
[25]J. S. Green, N. P. Dover, M. Borghesi, C. M. Brenner, F. H. Cameron, D. C. Carroll, P. S. Foster, P. Gallegos, G. Gregori, P. McKenna, C. D. Murphy, Z. Najmudin, C. A. J. Palmer, R. Prasad, L. Romagnani, K. E. Quinn, J. Schreiber, M. J. V. Streeter, S. Ter-Avetisyan1, O. Tresca, M. Zepf, and D. Neely, Plasma Phys. Controlled Fusion **56**, 084001 (2014).
[26]D. Batani, R. Jafer, M. Veltcheva, R. Dezulian, O. Lundh, F. Lindau, A. Persson, K. Osvay, C.-G. Wahlström, D. C. Carroll, P. McKenna, A. Flacco, and V. Malka, New J. Phys. **12**, 045018 (2010).
[27]S. Wilks, W. L. Kruer, M. Tabak, and A. B. Langdon, Phys. Rev. Lett. **69**, 1383 (1992).
[28]S. X. Luan, Y. Wei, M. Y. Yu, G. J. Ma, Q. J. Zhang, Z. M. Sheng, and M. Murakami, Phys. Plasmas **18**, 042701 (2011).
[29]A. A. Andreev, R. Sonobe, S. Kawata, S. Miyazaki, K. Sakai, K. Miyauchi, T. Kikuchi, K. Platonov, and K. Nemoto, Plasma Phys. Controlled Fusion **48**, 1605 (2006).
[30]V. M. Ovchinnikov, D. W. Schumacher, M. McMahon, E. A. Chowdhury, C. D. Chen, A. Morace, and R. R. Freeman, Phys. Rev. Lett. **110**, 065007 (2013).
[31]A. A. Andreev, A. Lévy, T. Ceccotti, C. Thaury, K. Platonov, R. A. Loch, and Ph. Martin, Phys. Rev. Lett. **101**, 155002 (2008).
[32]J. Schreiber, F. Bell, F. Grüner, U. Schramm, M. Geissler, M. Schnürer, S. Ter-Avetisyan, B. M. Hegelich, J. Cobble, E. Brambrink, J. Fuchs, P. Audebert, and D. Habs, Phys. Rev. Lett. **97**, 045005 (2006).
[33]C. Perego, A. Zani, D. Batani, and M. Passoni, Nucl. Instrum. Methods Phys. Res. A **653**, 89 (2011).
[34]J. F. Ziegler, M. D. Ziegler, and J. P. Biersack, Nucl. Instrum. Methods Phys. Res. B **268**, 1818 (2010).
[35]S. Ter-Avetisyan, M. Schnürer, P. V. Nickles, W. Sandner, T. Nakamura, and K. Mima, Phys. Plasmas **16**, 043108 (2009); **17**, 063101 (2010).